nature portfolio

https://doi.org/10.1038/s41586-022-05524-0

Supplementary information

Non-epitaxial single-crystal 2D material growth by geometric confinement

In the format provided by the authors and unedited

Supplementary Information

Non-epitaxial single-crystal 2D material growth by geometric confinement

Ki Seok Kim[1,2,†], Doyoon Lee[1,2,†], Celesta S. Chang[1,2,†], Seunghwan Seo[1,3], Yaoqiao Hu[4], Soonyoung Cha[5,6], Hyunseok Kim[1,2], Jiho Shin[1,2], Ju-Hee Lee[3], Sangho Lee[1,2], Justin S. Kim[7], Ki Hyun Kim[8], Jun Min Suh[1,2], Yuan Meng[7], Bo-In Park[1,2], Jung-Hoon Lee[9], Hyung-Sang Park[9], Hyun S. Kum[10], Moon-Ho Jo[5,11], Geun Young Yeom[8,12], Kyeongjae Cho[4], Jin-Hong Park[3,12*], Sang-Hoon Bae[7,13]* and Jeehwan Kim[1,2,14]*

[1]Research Laboratory of Electronics, Massachusetts Institute of Technology, Cambridge, MA 02139, USA.
[2]Department of Mechanical Engineering, Massachusetts Institute of Technology, Cambridge, MA 02139, USA.

[3]School of Electronic and Electrical Engineering Sungkyunkwan University, 2066 Seobu-ro, Jangan-gu, Suwon-si, Gyeonggi-do 16419, South Korea.

[4]Department of Materials Science and Engineering, The University of Texas at Dallas, Richardson, Texas 75080, USA.

[5]Center for Van der Waals Quantum Solids, Institute for Basic Science (IBS), Pohang 37673, South Korea.

[6]Department of Physics and Astronomy, University of California, Riverside, California 92521, United States.

[7]Department of Mechanical Engineering and Materials Science, Washington University in Saint Louis, MO 63130, USA.

[8]School of Advanced Materials Science and Engineering, Sungkyunkwan University, 2066 Seobu-ro, Jangan-gu, Suwon-si, Gyeonggi-do 16419, South Korea.

[9]ISAC Research, Inc. 340 Techno 2 ro, Yuseong gu, Daejeon, South Korea

[10]Department of Electrical and Electronic Engineering, Yonsei University, Seoul 03722, South Korea.

[11]Department of Materials Science and Engineering, Pohang University of Science and Technology (POSTECH), Pohang 37673, South Korea.

[12]SKKU Advanced Institute of Nano Technology (SAINT), Sungkyunkwan University, 2066 Seobu-ro, Jangan-gu, Suwon-si, Gyeonggi-do 16419, South Korea.

[13]Institute of Materials Science and Engineering, Washington University in Saint Louis, MO 63130, USA.

[14]Department of Materials Science and Engineering, Massachusetts Institute of Technology, Cambridge, MA 02139, USA.

[†]These authors contributed equally.

*Correspondence to jhpark9@skku.edu, sbae22@wustl.edu and jeehwan@mit.edu

1. Supplementary Notes

1.1 Confined single domain arrays growth mechanism of TMDs

Classical nucleation and growth theory states that materials growth on a substrate involves nucleation and growth processes. In our confined growth experiment of WSe_2, the formed WSe_2 clusters are first adsorbed onto the growth substrate and nucleate into small particles. The formed nucleation will then grow larger by continuously absorbing newly formed WSe_2 clusters. Therefore, one important factor that influences the nucleation and growth rate is the binding energy of WSe_2 clusters on the growth substrate. Thus, we calculated the binding energies of precusors W_3O_9 and Se_2 and product W_3Se_6 clusters on c-Al_2O_3 and a-SiO_2 substrates to find two materials with different critical Gibbs free energies. When using the CVD method with WO_3 and Se as precursors, there are two possible reaction mechanisms that can lead to WSe_2 growth[1]. The first mechanism is the on-substrate reaction (as shown in Fig. 1c). Volatile WO_3 (or reduced WO_3-xSe_x) evaporates and is deposited on the desired substrate, followed by selenium reduction and conversion into WSe_2. The second mechanism is the gas phase reaction. WO_3 and Se only react in the gas phase, in which the formed WSe_2 cluster diffuses onto the growth substrate for nucleation and growth. In terms of gas phase reaction, we have calculated the energetics of the following reactions:

$$W_3O_9 + 5.25\ Se_2 \rightarrow W_3Se_6 + 4.5SeO_2,\ \Delta G = 9.057\ eV\ (1)$$

$$W_3O_9 + 4.5\ Se_2 + 3H_2 \rightarrow W_3Se_6 + 3SeO_2 + 3H_2O,\ \Delta G = 4.644\ eV\ (2)$$

$$W_3O_9 + 3\ Se_2 + 9H_2 \rightarrow W_3Se_6 + 9H_2O,\ \Delta G = -4.181\ eV\ (3)$$

$$W_3O_9 + 9H_2 \rightarrow W_3 + 9H_2O,\ \Delta G = -4.181\ eV\ (4)$$

We can see that the Se reduction of WO_3 is only possible with the presence of H_2. This result is consistent with previous reports[2,3] and with our experimental observations. The negative Gibbs free energy change in reaction (3) suggests that gas phase reaction is involved and contributes to the CVD WSe_2 growth. The WSe_2 cluster formed in a gas phase is preferentially deposited onto c-Al_2O_3 and a-HfO_2 substrates due to stronger binding energy.

1.2 Growth methods for reproducibility of confined TMDs

For uniformity and reproducibility of confined TMDs, various parameters must be kept consistent. i) Since the selective growth of confined TMDs is carried out under atmospheric pressure, the air in the quartz tube must be completely removed with a vacuum pump and then filled with carrier gases (Ar/H_2) to sufficiently saturate the quartz tube. In addition, the connection part should be tightened as much as possible so that external air does not flow into the quartz tube during the growth process. ii) The external pressure/temperature must be kept constant. Minor changes can affect gas flow and increase/decrease

temperature during growth. iii) In the process of preparing samples and TMDs powder, one should be careful of external contamination sources as it can change the gas phase reaction during the synthesis process.

1.3 Characterization of device

To estimate the work function of confined BL-WSe_2, scanning probe microscopy measurements were performed in the non-contact Kelvin probe force microscopy (KPFM) modes using an NX10 system (Park Systems Corp.). KPFM measurements were performed under dark and ambient conditions using a platinum/iridium (Pt/Ir)-coated Si tip. In the KPFM measurements, the surface work function of the sample (Φ_{sample}) was obtained using the following equations:

$$\Phi_{sample} = eV_{CPD1} - eV_{CPD2} + \Phi_{HOPG},$$
$$V_{CPD1} = V_{CPD\_tip} - V_{CPD\_sample},$$
$$V_{CPD2} = V_{CPD\_tip} - V_{CPD\_HOPG},$$
$$\Phi_{sample} = e(V_{HOPG} - V_{sample}) + \Phi_{HOPG}.$$

Here, V_{CPD1} is the contact potential difference (CPD) between the tip and the sample, and V_{CPD2} is CPD between the tip and the highly oriented pyrolytic graphite (HOPG), respectively. Φ_{HOPG} denotes the work function of HOPG; the HOPG is conventionally used to calibrate the work function of the KPFM tip because it has a clean surface and its work function is well known to be 4.6 eV[4]. To determine the Schottky barrier height between Pt source/drain electrodes and confined BL-WSe_2, the electrical characterization with respect to temperature was performed with an Agilent 4155C under vacuum. Then, a thermionic emission current equation for a Pt-WSe_2-Pt junction was used as follows:

$$I_0 = AA^{**}T^2 \exp\left(\frac{-q\Phi_B}{k_B T}\right)\left[\exp\left(\frac{qV_{DS}}{nk_B T}\right) - 1\right],$$

where I_0 is the saturation current, A is the effective area, A^{**} is the Richardson constant, T is the temperature in Kelvin, q is the elementary charge, Φ_B is the Schottky barrier height, k_B is the Boltzmann constant, V_{DS} is the voltage across the source and drain, and n is the ideality factor. When a reverse bias is applied, the $\exp\left(\frac{qV_{DS}}{nk_B T}\right)$ term becomes ignorable and the above equation can be simplified as follows:

$$I_0 = -AA^{**}T^2 \exp\left(\frac{-q\Phi_B}{k_B T}\right) .$$

Moving the T^2 term to the left-hand side of the equation and taking the natural log on both sides, the following equation was obtained

$$\ln\left(\frac{I_0}{T^2}\right) = \ln\left(AA^{**}\right) - \frac{q\Phi_B}{k_B T} \ .$$

Because WSe_2 FET operates under thermionic emission and diffusion mechanisms, a conventional Richardson plot does not give a linear fit over the entire temperature range. Thus, we employed a modified Richardson plotting method based on a thermionic emission-diffusion model[5]. The linearity in the $\ln(I_0/T^2) - q^2\sigma_0^2/2(k_BT)^2$ versus q/k_BT plot was obtained, where σ_0 is the standard deviation of the Gaussian distribution. From the slope in the modified Richardson plot, the hole barrier height was estimated (Supplementary Fig. 10).

2. Supplementary Figures

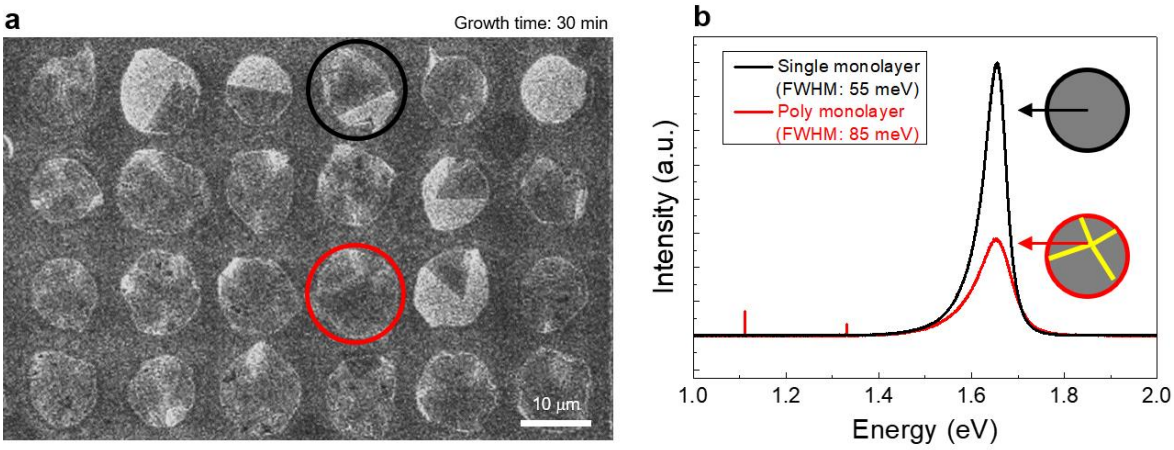

Supplementary Fig. 1 | Comparison of confined single- and poly-monolayer WSe_2. a, SEM morphology and **b,** PL characteristics of confined single- and poly-monolayer WSe_2 in 10 mm-sized sapphire pockets.

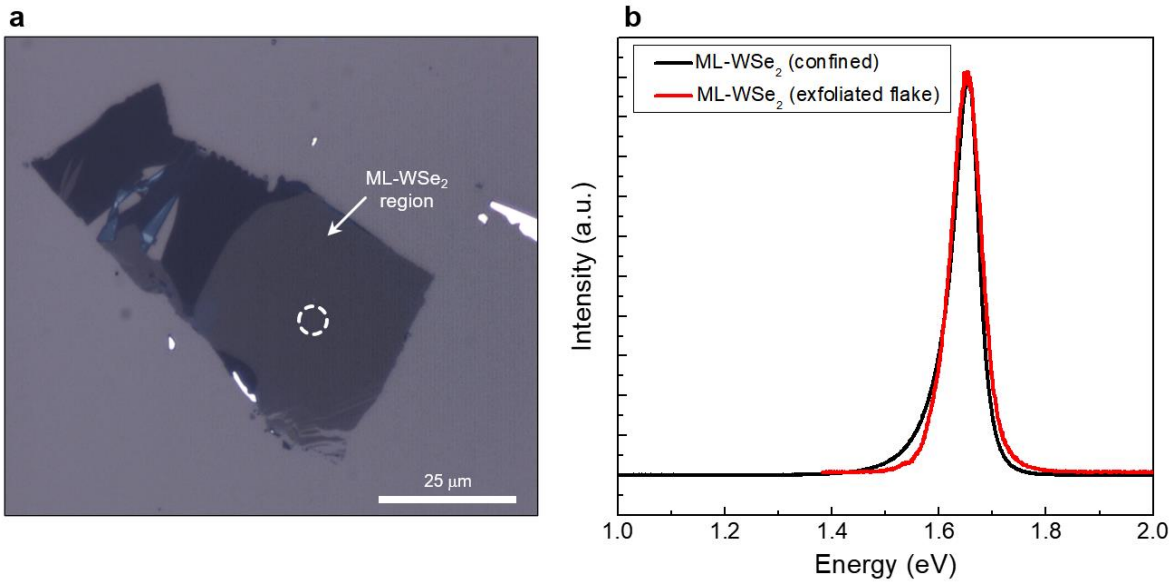

Supplementary Fig. 2 | PL spectra of ML-WSe_2. a, Optical microscopy (OM) image of an as-exfoliated ML-WSe_2 flake transferred onto SiO_2 substrate, wherein circular mark indicates laser-irradiated spot. **b,** PL spectra of confined ML-WSe_2 film (black) and as-exfoliated ML-WSe_2 flake (red), respectively.

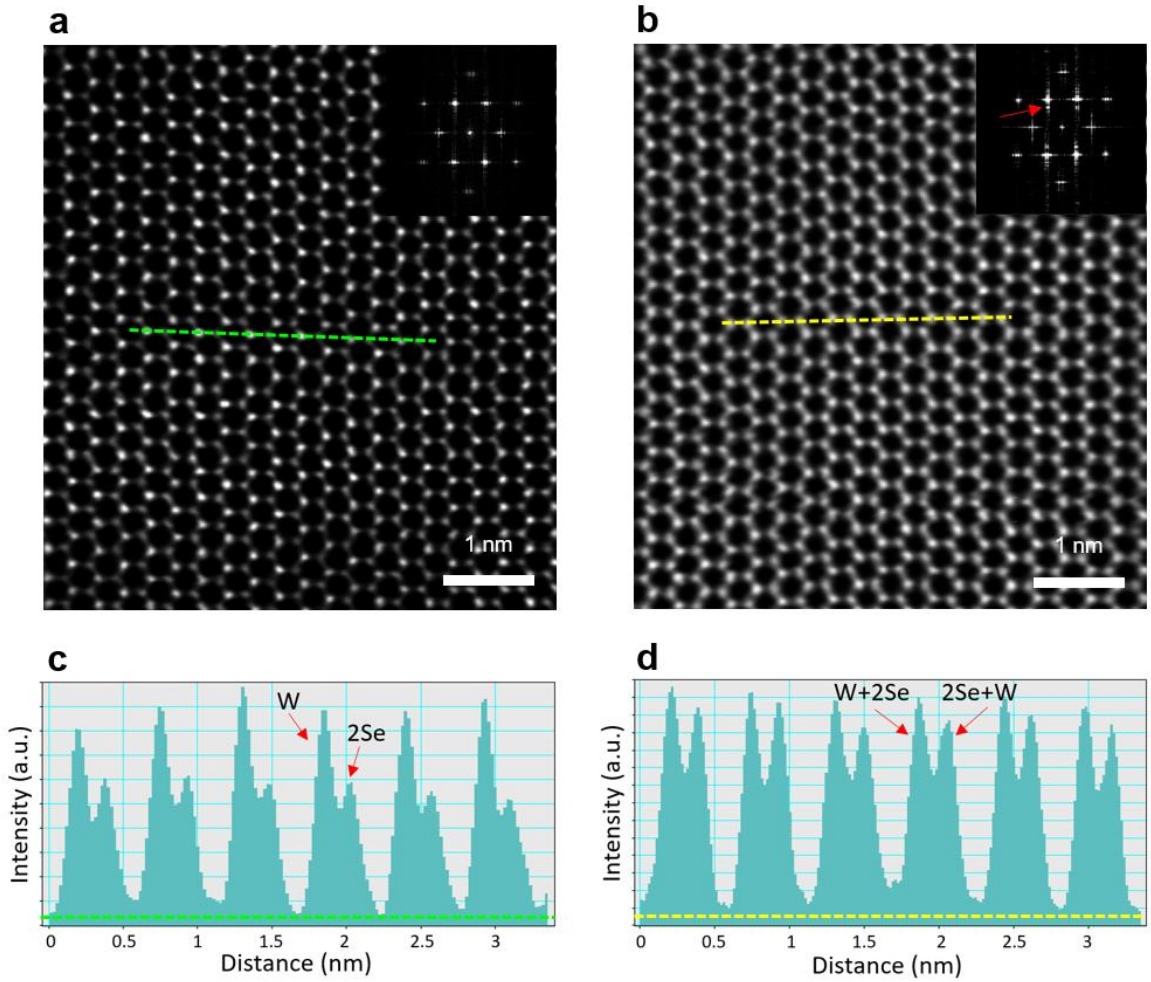

Supplementary Fig. 3 | Plan-view HAADF-STEM analysis of layer-by-layer confined growth of WSe_2. a–d, Plan-view HAADF-STEM images of confined ML- (**a**) and BL-WSe_2 (**b**). The inset FFT pattern shows the difference between ML-WSe_2 and AA′ stacked BL-WSe_2 (**a, b**). The FFT pattern peak was split into two due to the coexistence of W and 2Se in the same atomic arrangement [red arrow in (**b**)]. Confined ML- and BL-WSe_2 were also compared by line intensity profiling (**c, d**) each extracted from green line in (**a**) and yellow line in (**b**).

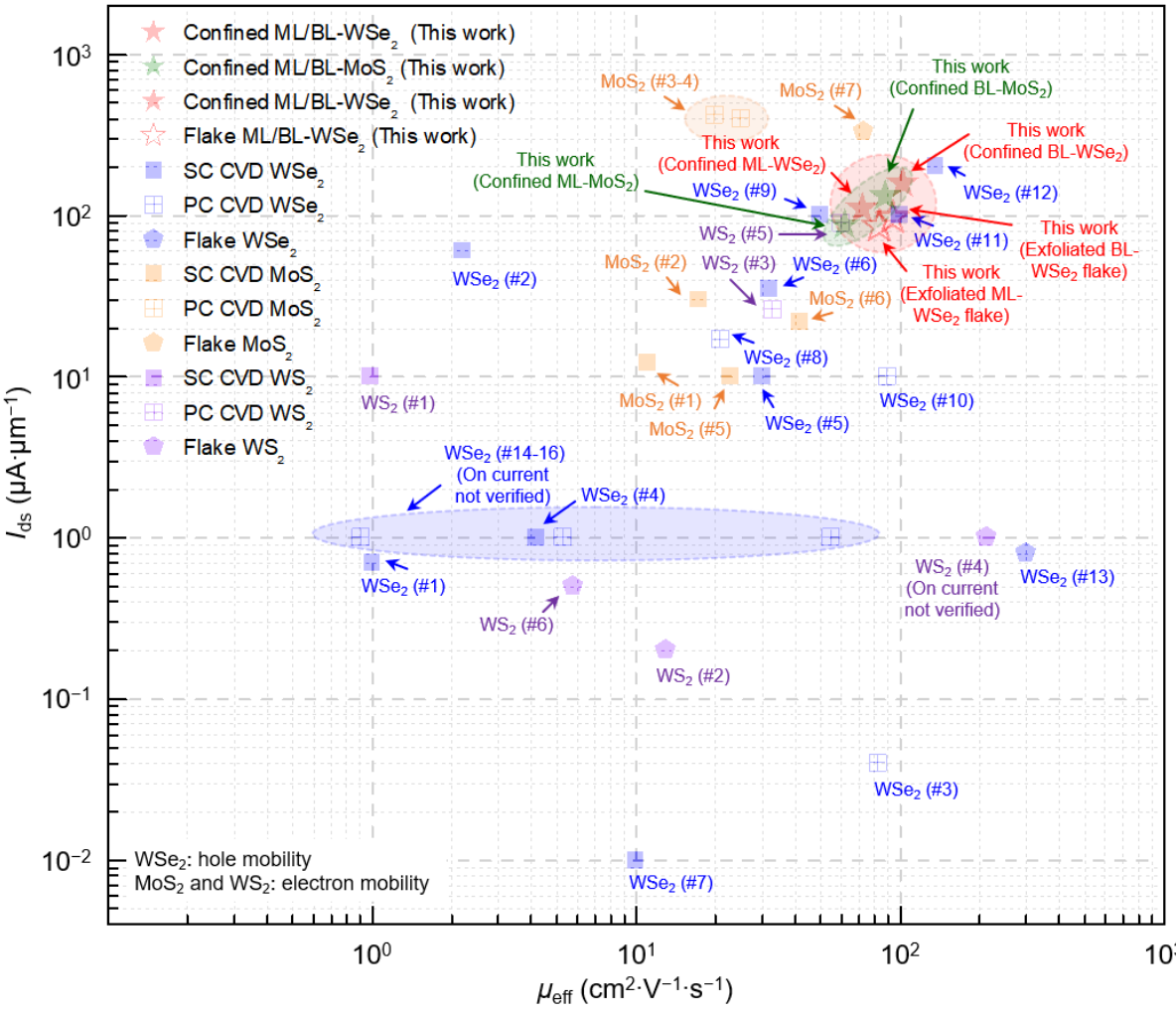

Supplementary Fig. 4 | Benchmark for various types (CVD grown single-crystalline, CVD grown poly-crystalline, and exfoliated flake) of TMDs (WSe_2, MoS_2, WS_2, and others) with respect to field-effect mobility and on current density. Numbers in parentheses (#Number) denote device label; (see Supplementary Table 1 for details).

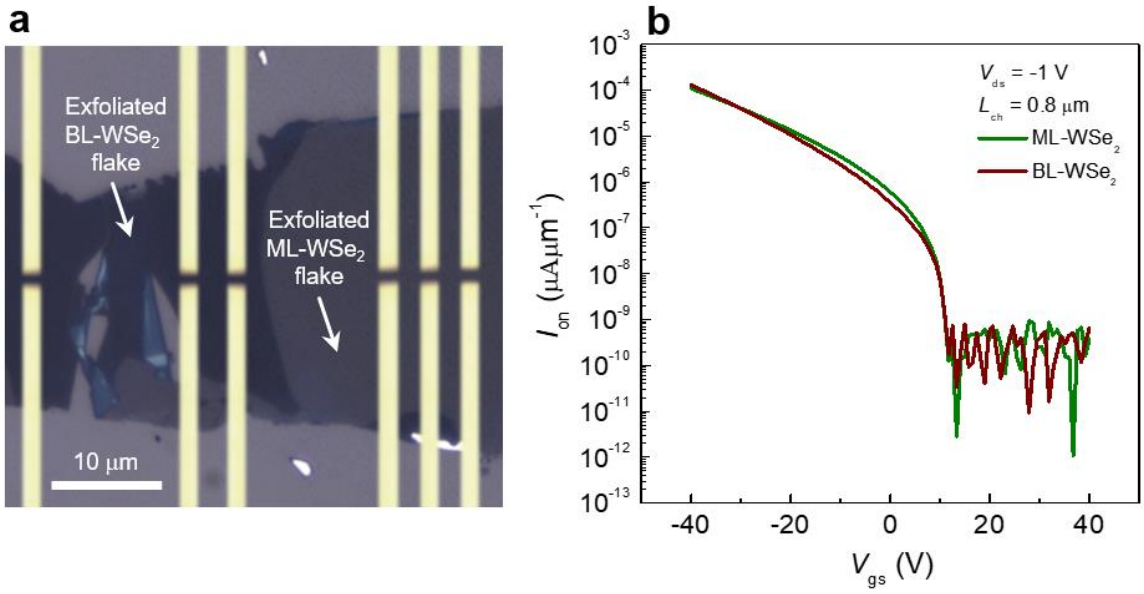

Supplementary Fig. 5 | Characterization of FETs fabricated with as-exfoliated ML/BL-WSe_2 flake. a, OM image of FETs fabricated with as-exfoliated ML/BL-WSe_2 flake. **b,** Transfer characteristics of FET fabricated with as-exfoliated ML-WSe_2 (olive-color) flake and BL-WSe_2 flake (wine-color) at V_{DS} = –1 V, respectively.

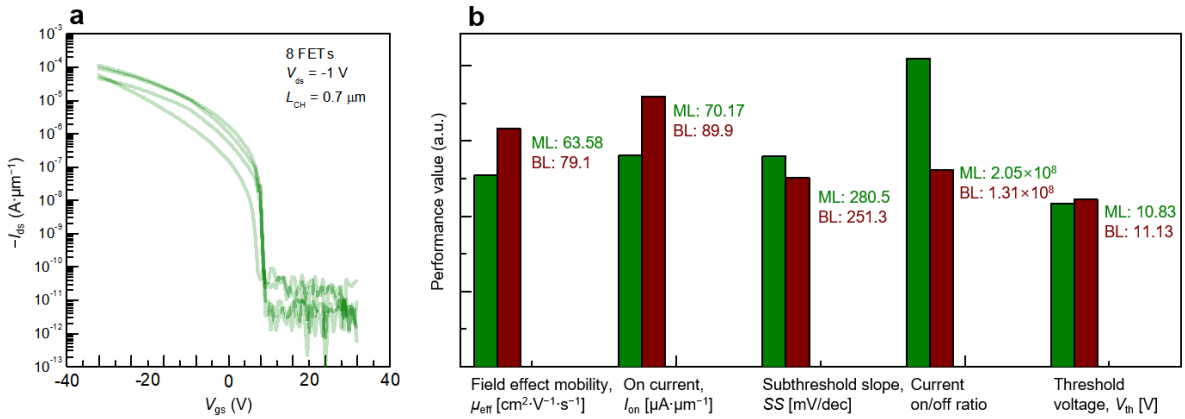

Supplementary Fig. 6 | Electrical characterization of FETs fabricated with confined ML-WSe_2. a, Transfer characteristics of 4 FETs fabricated with confined ML-WSe_2. **b,** Comparison of electrical performances between FETs fabricated with confined ML-WSe_2 (olive-color) and confined BL-WSe_2 (wine-color), where performances include field-effect mobility, on current, subthreshold slope, current on/off ratio, and threshold voltage. Here, denoted values in the graph are those of average, respectively.

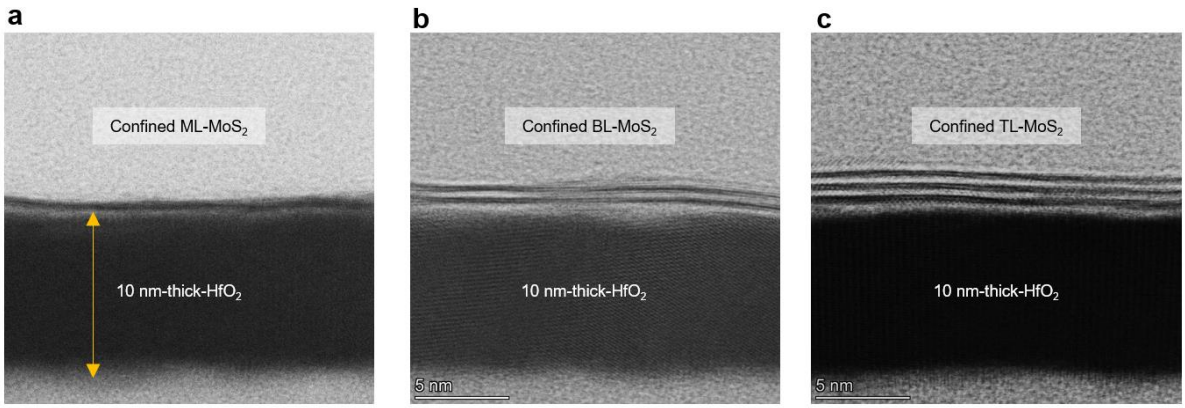

Supplementary Fig. 7 | MoS_2 layer grown on a-HfO_2 patterned with a-SiO_2 trenches. a–c, HAADF-STEM images of confined ML-, BL-, and trilayer (TL)-MoS_2 obtained by layer-by-layer growth on a-HfO_2 pockets.

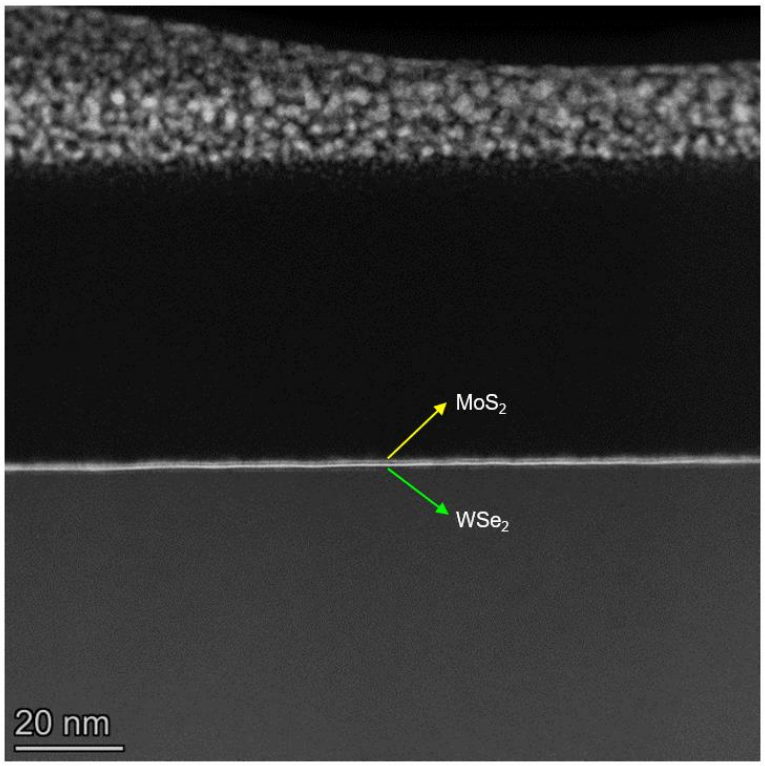

Supplementary Fig. 8 | STEM image acquired at low magnification. Uniform heterointerface without secondary nucleation was observed over a relatively large area in confined ML-MoS_2 / ML-WSe_2.

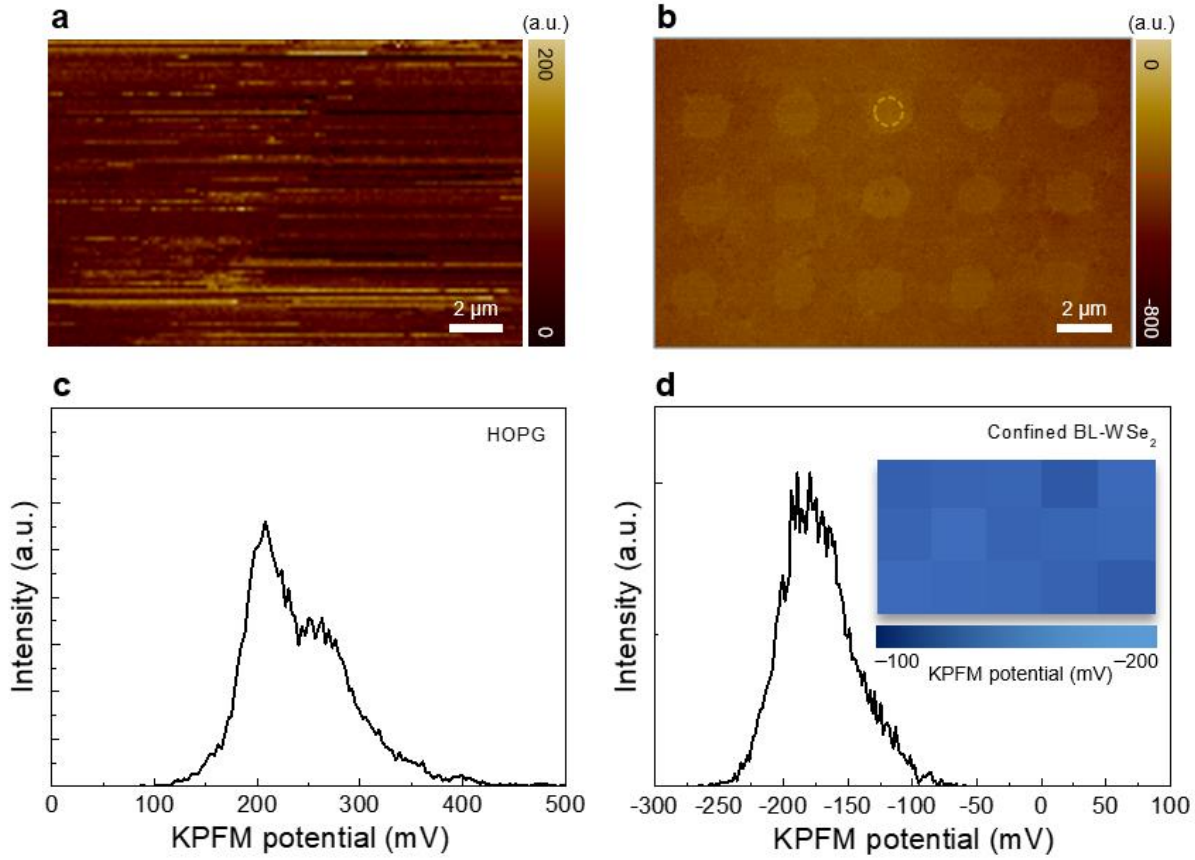

Supplementary Fig. 9 | KPFM analysis on confined BL-WSe_2. a, b, KPFM mapping image of HOPG sample (**a**) and confined BL-WSe_2 (**b**). **c, d,** KPFM potential profile of HOPG sample (**c**) and confined BL-WSe_2 (**d**). Here, inset color map shows KPFM potential distribution observed in confined BL-WSe_2 depicted in (**b**).

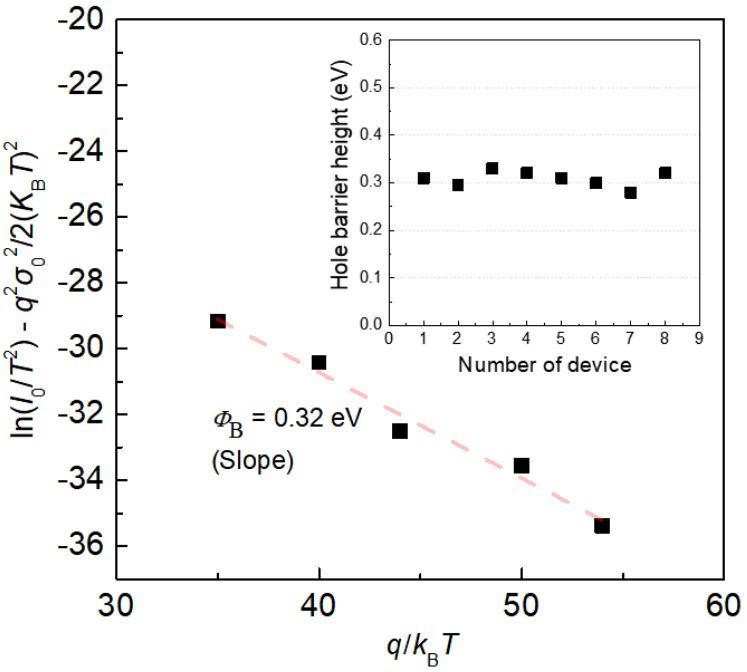

Supplementary Fig. 10 | Modified Richardson plot method for extracting hole barrier height. Inset shows hole barrier height distribution extracted from 8 FETs.

3. Supplementary Table

Label	Channel			Gate stack	S/D Contact	I_{on} ($\mu A \cdot \mu m^{-1}$)	μ_{eff} ($cm^2 \cdot V^{-1} \cdot s^{-1}$)	I_{on}/I_{off}	SS (mV/dec)	Ref.
	Material	L_{CH} (μm)	W_{CH} (μm)							
Confined BL-WSe_2 (This work)	Single-crystalline bilayer WSe_2	0.7~1	1	300 nm SiO_2	10 nm Pt/ 80 nm Au	155.8	103.5	$>10^8$	240.5	-
Confined ML-WSe_2 (This work)	Single-crystalline monolayer WSe_2	0.7~1	1	300 nm SiO_2	10 nm Pt/ 80 nm Au	108.1	72.8	$>10^8$	280.5	-
Confined BL-MoS_2 (This work)	Single-crystalline bilayer MoS_2	0.7~1	1	300 nm SiO_2/10 nm HfO_2	10 nm Ni/ 80 nm Au	129.3	88.6	$>10^7$	290.38	-
Confined ML-MoS_2 (This work)	Single-crystalline monolayer MoS_2	0.7~1	1	300 nm SiO_2/10 nm HfO_2	10 nm Ni/ 80 nm Au	86.7	62.2	$>10^8$	320.16	-
WSe_2 flake (This work)	Exfoliated monolayer WSe_2 flake	0.7~1	1	300 nm SiO_2	10 nm Pt/ 80 nm Au	110.3	84.3	$>10^8$	~300	-
WSe_2 flake (This work)	Exfoliated bilayer WSe_2 flake	0.7~1	1	300 nm SiO_2	10 nm Pt/ 80 nm Au	130.8	94.6	$>10^8$	~300	-
WSe_2 (#1)	Single-crystalline CVD monolayer WSe_2 film	1	5	50 nm Al_2O_3	40 nm Ni/ 30 nm Au	~0.7	1	10^6	Not verified	6
WSe_2 (#2)	Single-crystalline CVD trilayer WSe_2 film	Not verified	Not verified	300 nm SiO_2	30 nm Pd	~60	2.2	10^6	Not verified	7
WSe_2 (#3)	Poly-crystalline CVD monolayer WSe_2 film	Not verified	Not verified	*h*-BN	0.5 nm Ti/ 50 nm Pd	0.04	83	10^7	Not verified	8
WSe_2 (#4)	Single-crystalline CVD monolayer WSe_2 film	1	5	100 nm SiO_2	40 nm Ni/ 30 nm Au	1	4.2	Not verified	Not verified	9
WSe_2 (#5)	Single-crystalline CVD bilayer WSe_2 film	10 to 0.75	24	PEO: $CsClO_4$	25 nm Ni & 10 nm/10 nm Pd/Au	1−10	30	10^7	~200	10
WSe_2 (#6)	Single-crystalline CVD bilayer WSe_2 film	3 to 0.23	Not verified	20 nm HfO_2	20 nm Ni/ 60 nm Au	42	22−32	$>10^8$	Not verified	11
WSe_2 (#7)	Single-crystalline CVD bilayer WSe_2 film	1.8−2	10	285 nm SiO_2 or 70 nm SiN_x	Cr/Au	0.01	10	10^4	Not verified	12
WSe_2 (#8)	Poly-crystalline CVD monolayer WSe_2 film	Not verified	Not verified	285 nm SiO_2	1 nm Ti/ 50 nm Au	17	21	$>10^5$	Not verified	13
WSe_2 (#9)	Single-crystalline CVD monolayer WSe_2 film	1	Not verified	300 nm SiO_2	100 nm Au	100	100	10^8	Not verified	14
WSe_2 (#10)	Poly-crystalline CVD monolayer WSe_2 film	668	1225	PS-PMMA-PS	2 nm Ni/ 70 nm Au	10	90	10^5	Not verified	15
WSe_2 (#11)	Single-crystalline CVD monolayer WSe_2 film	5	30	SiO_2	Pt	100	90	$>10^6$	Not verified	16
WSe_2 (#12)	Single-crystalline CVD bilayer WSe_2 film	1.8	10	70 nm SiN_x	VdW contact	150 up to 900	137	$>10^7$	Not verified	12
WSe_2 (#13)	Exfoliated WSe_2 flake (12L, 8 nm)	15.8	7.7	270 nm SiO_2	3 nm Ti/ 90 nm Au	0.8	302	10^6	Not verified	17
WSe_2 (#14)	Poly-crystalline TAC WSe_2 film (~21L)	3	80	300 nm SiO_2	10 nm Ti/ 100 nm Au	Not verified	0.91	2.2	Not verified	18
WSe_2 (#15)	Poly-crystalline CVD bilayer WSe_2 film	Not verified	Not verified	Not verified	5 nm Cr/ 40 nm Au	Not verified	5.3	$>10^4$	Not verified	19

WSe_2 (#16)	Poly-crystalline CVD monolayer WSe_2 film	Not verified	Not verified	PS-PMMA-PS	2 nm Ni/ 80 nm Au	Not verified	55	$>10^5$	60−130	20
MoS_2 (#1)	Single-crystalline CVD monolayer MoS_2 film	1	Not verified	285 nm SiO_2	Ti/Au	12.1	11.1	Not verified	Not verified	21
MoS_2 (#2)	Single-crystalline CVD bilayer MoS_2 film	1	3.6	300 nm SiO_2	5 nm Cr/ 45 nm Pd	30	17.3	$\sim 10^8$	Not verified	22
MoS_2 (#3)	Poly-crystalline CVD mono-bilayer MoS_2 film	2 to 0.1	5	8 nm HfO_2 (bottom)/ TiN/ 2 nm Al_2O_3/6 nm HfO_2 (top)	Ni/Pd	420	20	$>10^8$	109	23
MoS_2 (#4)	Poly-crystalline CVD bilayer MoS_2 film	2 to 0.16	2.7	15 nm HfO_2	20 nm Ni/ 20 nm Au	400	25	Not verified	Not verified	24
MoS_2 (#5)	Single-crystalline CVD mono-bilayer MoS_2 film	47 nm to 30 nm	115 nm	12 nm HfO_2	Not verified	10 up to 100	4−23	Not verified	80	25
MoS_2 (#6)	Single-crystalline CVD monolayer MoS_2 film	8.6 to 5	11.6	30 nm SiO_2	2 nm Ti/ 40 nm Au	22	42	$>10^6$	Not verified	26
MoS_2 (#7)	Exfoliated MoS_2 flake (4-5L)	5	Not verified	255 nm SiO_2	15 nm Ni/ 50 nm Au	330	73	10^8	65	27
WS_2 (#1)	Single-crystalline CVD monolayer WS_2 film	3	3	50 nm Al_2O_3	10 nm Ti/ 50 nm Au	10	0.99	10^7	Not verified	28
WS_2 (#2)	Exfoliated WS_2 flake (23L, 18 nm)	3	6	90 nm SiO_2	Ti/Au	0.2	13	Not verified	Not verified	29
WS_2 (#3)	Poly-crystalline CVD monolayer WS_2 film	5−100	5	Al_2O_3 or SiO_2	Ni/Au	26	33	10^7	100−400	30
WS_2 (#4)	Exfoliated monolayerWS_2 flake	Not verified	Not verified	300 nm SiO_2	60 nm Al/ 40 nm Au	Not verified	214	$\sim 10^6$	Not verified	31
WS_2 (#5)	Poly-crystalline CVD 5-7 layer WS_2 film	0.1	1	90 nm SIO_2	30 nm Ni/ 60 nm Au	90	60	$\sim 10^5$	Not verified	32
WS_2 (#6)	Exfoliated monolayer WS_2 flake	1.5	2	SiO_2	6 nm Cr/ 30 nm Au	0.465	5.8	$\sim 10^6$	Not verified	33

Supplementary Table 1 | Benchmark table for FETs fabricated with various types of TMDs.

Supplementary References

1. Zhou, D. *et al.* Unveiling the growth mechanism of MoS_2 with chemical vapor deposition: from two-dimensional planar nucleation to self-seeding nucleation. *Cryst. Growth Des* **18**, 1012–1019 (2018).
2. Huang, J. K. *et al.* Large-area synthesis of highly crystalline WSe_2 monolayers and device applications. *ACS Nano* **8**, 923–930 (2014).
3. Tsirlina, T. *et al.* Synthesis and characterization of inorganic fullerene-like WSe_2 material. *Fullerene Sci. Technol.* **6**, 157–165 (1998).
4. Jin, G. *et al.* Heteroepitaxial van der Waals semiconductor superlattices. *Nat. Nanotechnol.* **16**, 1092–1098 (2021).
5. Lin, Y.-F. *et al.* Barrier inhomogeneities at vertically stacked graphene-based heterostructures. *Nanoscale* **6**, 795-799 (2014).
6. Kozhakhmetov, A. *et al.* Scalable substitutional re-doping and its impact on the optical and electronic properties of tungsten diselenide. *Adv. Mater.* **32**, 2005159 (2020).
7. Park, K. *et al.* Uniform, large-area self-limiting layer synthesis of tungsten diselenide. *2D Mater*. **3**, 014004 (2016).
8. Liu, B. *et al.* High-performance WSe_2 field-effect transistors via controlled formation of in-plane heterojunctions. *ACS Nano* **10**, 5153–5160 (2016).
9. Zhang, X. *et al.* Defect-controlled nucleation and orientation of WSe_2 on hBN: a route to single-crystal epitaxial monolayers. *ACS Nano* **13**, 3341–3352 (2019).
10. Lin, Y.-C. *et al.* Realizing large-scale, electronic-grade two-dimensional semiconductors. *ACS Nano* **12**, 965–975 (2018).
11. Wang, X. *et al.* High-performance n-type transistors based on CVD-grown large-domain trilayer WSe_2. *APL Mater*. **9**, 071109 (2021).
12. Li, J. *et al.* General synthesis of two-dimensional van der Waals heterostructure arrays. *Nature* **579**, 368–374 (2020).
13. Chen, M. *et al.* Gold-vapor-assisted chemical vapor deposition of aligned monolayer WSe_2 with large domain size and fast growth rate. *Nano Research* **13**, 2625–2631 (2020).
14. Zhou, H. *et al.* Large area growth and electrical properties of p-type WSe_2 atomic layers. *Nano Lett.* **15**, 709–713 (2015).
15. Huang, J.-K. *et al.* Large-area synthesis of highly crystalline WSe_2 monolayers and device application. *ACS Nano* **8**, 923–932 (2014).
16. Zhang, Z. *et al.* Ultrafast growth off large single crystals of monolayer WS_2 and WSe_2. *National Sci. Rev.* **7**, 737–744 (2020).
17. Pradhan, N. R. *et al.* Hall and field-effect mobilities in few layered p-WSe_2 field-effect transistors. *Sci. Rep.* **5**, 8979 (2015).
18. Kim, W. *et al.* Field-dependent electrical and thermal transport in polycrystalline WSe_2. *Adv. Mater. Interfaces* **5**, 1701161 (2018).
19. Mandyam, S. V. *et al.* Controlled growth of large-area bilayer tungsten diselenides with lateral P-N junctions. *ACS Nano* **13**, 10490–10498 (2019).
20. Pu, J. *et al.* Highly flexible and high-performance complementary inverters of large-area transition metal dichalcogenide monolayers. *Adv. Mater.* **28**, 4111–4119 (2016).
21. Liu, H. *et al.* Statistical study of deep submicron dual-gated field-effect transistors on monolayer chemical vapor deposition molybdenum disulfide films. *Nano Lett.* **13**, 2640–2646 (2013).
22. Wu, W. *et al.* High mobility and high on/off ratio field-effect transistors based on chemical vapor deposited single-crystal MoS_2 grains. *Appl. Phys. Lett.* **102**, 142106 (2013).

23. Wu, X. *et al.* Dual gate synthetic WS_2 MOSFETs with 120 μS/μm G_m 2.7 μF/μm^2 capacitance and ambipolar channel. *2021 IEEE International Electron Devices Meeting (IEDM)* PP. 3.6.1–3.6.4 (2020).
24. Xiong, X. *et al.* Demonstration of vertically-stacked CVD monolayer channels: MoS_2 nanosheets GAA-FET with I_{on}>700 μA/μm and MoS_2/WSe_2 CFET. *2021 IEEE International Electron Devices Meeting (IEDM)* PP. 7.5.1–7.5.4 (2021).
25. Smets, Q. *et al.* Sources of variability in scaled MoS_2 FETs. *2020 IEEE International Electron Devices Meeting (IEDM)* PP. 3.1.1–3.1.4 (2020).
26. Smithe, K. K. H. *et al.* Low variability in synthetic monolayer MoS_2 devices. *ACS Nano* **11**, 8459–8463 (2017).
27. Wang, J. *et al.* High mobility MoS_2 transistor with low Schottky barrier contact by using Atomic thick h-BN as a tunneling layer. *Adv. Mat.* **28**, 8302–8308 (2016).
28. Gao, Y. *et al.* Large-area synthesis of high-quality and uniform monolayer WS_2 on reusable Au foils. *Nat. Commun.* **6**, 8569 (2015).
29. Kim, Y. J. *et al.* Contact resistance reduction of WS_2 FETs using high-pressure hydrogen annealing. *J. of the Elect. Device Soc.* **6**, 164–168 (2018).
30. Sebastian, A. *et al.* Benchmarking monolayer MoS_2 and WS_2 field-effect transistors. *Nat. Commun.* **12**, 693 (2021).
31. Iqbal, M. W. *et al.* High-mobility and air-stable single-layer WS_2 field-effect transistors sandwiched between chemical vapor deposition-grown hexagonal BN films. *Sci. Rep.* **5**, 10699 (2015).
32. Yang, L. *et al.* Chloride molecular doping technique on 2D materials: WS_2 and MoS_2 *Nano Lett.* **14**, 6275–6280 (2014).
33. Iqbal, M .W. *et al.* Tailoring the electrical and photo-electrical properties of a WS_2 field effect transistor by selective n-type chemical doping. *RSC Adv.* **6**, 24675 (2016).